Fuel Cells

WILEY-VCH

SPECIAL ISSUE EFCF2023 - Special Issue on “Fuel Cells, Electrolyzers & Electrochemical Reactors, CO_2 Emission Reduction & Reuse”

Fuel Cells FROM FUNDAMENTALS TO SYSTEMS

RESEARCH ARTICLE OPEN ACCESS

Lanthanum-Nickel-Based Mixed-Oxide-Coated Nickel Electrodes for the OER Electrocatalysis

Nikolas Mao Kubo[1] | Rim Mhamdi[1] | Regina Palkovits[1,2]

[1]Institute of Technical and Macromolecular Chemistry, RWTH Aachen University, Aachen, Germany | [2]Institute for a Sustainable Hydrogen Economy, Forschungszentrum Jülich, Jülich, Germany

Correspondence: Regina Palkovits (palkovits@itmc.rwth-aachen.de)

Received: 18 December 2023 | **Revised:** 12 March 2024 | **Accepted:** 29 May 2024

Guest Editors: M. H. Eikerling | O. Bucheli | P. Bele

Funding: This study was supported by Federal Ministry of Education and Research, Grant/Award Numbers: H2Giga QT1.1 PrometH2eus, FKZ 03HY105A

Keywords: alkaline water electrolysis (AWE) | electrocatalysis | nickel oxide | oxygen evolution reaction (OER) | perovskite | water splitting

ABSTRACT

The anodic oxygen evolution reaction (OER) remains a bottleneck for electrocatalytic water splitting due to its sluggish kinetics and, thus, high overpotentials. This limits water electrolysis as a key technology for the generation of hydrogen as a sustainable alternative to fossil fuels. For alkaline water splitting, perovskite phases (ABO_3) with earth-abundant first-row transition-metals have emerged as a promising material class for OER electrocatalysts. Among these, $LaNiO_3$ has been found to exhibit high intrinsic OER activity. To increase catalyst utilization, a high surface area of the catalyst is desirable and can be achieved by impregnation of porous templates. In this work, La–Ni-based oxides were prepared via impregnation of activated carbon and subsequent heating, combining precursor calcination and template removal into one step. The phase structure of the samples is analyzed via powder X-ray diffractometry, and the morphology is determined by scanning electron microscopy. The synergistic effect of B-site mixing iron as well as A-site mixing strontium into $LaNiO_3$ is studied and found to increase its OER activity, confirming the activity-enhancing effect of Fe in Ni-based OER electrocatalysts. To allow for facile technical application of the catalysts, the electrodes are prepared by coating a perovskite ink onto Ni-metal as industrially relevant substrates, followed by calcination.

1 | Introduction

Hydrogen is a sustainable and ecologically friendly alternative energy carrier to the limited fossil fuels when produced from renewable sources [1–3]. A key technology for the generation of such hydrogen is water electrolysis powered by renewable energy sources. This hydrogen can be used as chemical energy storage to solve the shift between the demand and intermittent production of renewable energy and serve as a chemical feedstock in a possible hydrogen society [1–6]. The electrolysis of water (water splitting) consists of two half-cell reactions, the cathodic reduction toward H_2 (hydrogen evolution reaction) and the anodic oxidation toward O_2 (oxygen evolution reaction [OER]), and takes place at an equilibrium potential of $E^0 = 1.23$ V. Although both reactions require overpotentials to take place, especially the OER poses the limiting bottleneck to the water-splitting technology. The evolution of oxygen stoichiometrically requires four electrons and proceeds according to the following equation in alkaline media where the hydroxyl anion represents the main charge carrier:

$$4OH^- \rightarrow O_2 + 2H_2O + 4e^- \quad (1)$$

Paper presented at the 27th International Conference in Series (EFCF2023) featuring the 5th International MEEP Symposium, held 4–7 July 2023 in Lucerne, Switzerland. Organized by the European Fuel Cell Forum, www.efcf.com.

This four-electron transfer and the formation of the oxygen–oxygen bond is thermodynamically challenging and the sluggish kinetics result in high overpotentials required [7–11].

In order to find suitable electrocatalysts, iridium- and ruthenium oxide-based materials have been identified early to exhibit low overpotentials [12, 13]. However, research efforts have been made to develop transition metal-based OER electrocatalysts independent of precious metals to allow for large-scale application of the water-splitting technology. Materials based on the earth-abundant elements iron, cobalt, and especially nickel show high activity and stability in alkaline water splitting [14–17]. Among different oxidic material classes, perovskites provide a promising crystal lattice platform due to their wide compositional variability and stability as well as finely tunable properties [18–20]. Perovskite oxides follow the general structure ABO_3 where A is a larger and B a smaller cation. Here, $LaNiO_3$ was found to exhibit high OER electrocatalytic activity among the first-row transition-metal-based perovskites [21, 22]. Furthermore, the activity of perovskites can be tuned by mixing different cations to either the A- or B-site or both sites. Generally, the presence of iron exerts a beneficial effect on the activity of Ni-based OER catalysts [23–26]. For $LaNiO_3$, Chiba et al. discovered an increase in conductivity in the $LaNi_{1-x}Fe_xO_3$ ($0 < x < 1$) with the maximum at about $x = 0.4$ [27]. However, only few reports can be found on the application of different $LaNi_{1-x}Fe_xO_3$ phases as OER catalysts. Here, the studies from Zhang et al. [28], Gozzo et al. [29], Bak et al. [30], and Le Wang et al. [31] report an enhancement of OER activity with the incorporation of Fe into the $LaNiO_3$ host lattice. Each report investigates different values for x and applies different electrochemical testing protocols, exacerbating the determination of an optimum Ni/Fe-ratio in the $LaNi_{1-x}Fe_xO_3$ phases. However, these reports concur in reporting an activity maximum below or around $x = 0.5$ and lower activities for both unmixed phases $LaNiO_3$ or $LaFeO_3$ [28–31]. Adolphsen et al. in contrast found a lower activity for the Fe-incorporated nickelate; however, this composition exhibited increased phase stability [32]. Furthermore, oxygen vacancies are reported to play a crucial role in oxide-based OER electrocatalysts by facilitating elemental mechanistic steps [33]. In perovskite oxides, this can be achieved by A-site doping with undervalent dopants such as Sr^{2+} in the case of ferrites and cobaltites, which results in an oxygen non-stoichiometry and, thus, in the formation of oxygen vacancies [34–40].

In order to allow for large application of OER electrocatalysts in the foreseeable future, it is necessary to implement economically feasible synthesis routes and apply industrially relevant testing conditions already during catalyst development based on literature-known high-performing materials. A further step to facilitate technical utilization of electrocatalysts is their investigation directly applied on industrially relevant substrates such as nickel or nickel-based alloys [40, 41]. In this work, a facile synthesis approach is used to prepare lanthanum-nickel-based perovskites as OER electrocatalyst. The catalyst material usage can be maximized with large surface areas and, thus, large electrode-electrolyte-interfaces through syntheses yielding rough particle surfaces, porosity, and small particle sizes. Following the protocol of Schwickardi et al., activated carbon is used here as a template to transfer its highly porous structure onto the perovskite particles [42]. The activated carbon is impregnated with dissolved metal salt precursors and then heated in air. During this heat treatment, the precursors are calcined to the metal oxides. Simultaneously, the templating carbon is combusted, leaving carbon-free metal oxides. Therefore, the application of activated carbon as templating material allows the combination of precursor calcination and template removal into one step. With this method, a series of La–Ni–Fe-oxide materials with the respective stoichiometric La/Ni/Fe ratios of 1:$(1 - x)$:x with $x = 0$ (LN), 0.2 (LNF82), 0.4 (LNF64), 0.6 (LNF46), 0.8 (LNF28), and 1.0 as well as a La–Sr–Ni-oxide with a La/Sr ratio of 8:2 (LS82N) is prepared. The crystallographic phase structures of all samples are determined via powder X-ray diffractometry (XRD), and their morphology visualized with scanning electron microscopy (SEM). The materials are applied as inks onto nickel electrodes and then electrochemically tested in the alkaline OER electrocatalysis.

2 | Experimental Procedures

2.1 | Catalyst Preparation and Characterization

Activated carbon (NORIT CN1, Thermo Scientific), nickel foil (Alfa Aesar, 0.5 mm thickness, annealed, 99.5%), $La(NO_3)_3{\cdot}6\,H_2O$ (Sigma-Aldrich, 99.99%), $Ni(NO_3)_2{\cdot}6\,H_2O$ (Merck, EMSURE ACS), $Fe(NO_3)_3{\cdot}9\,H_2O$ (Sigma-Aldrich, ≥98%), $Sr(NO_3)_2$ (Roth, ≥99%), Terpineol (Sigma-Aldrich, mixture of isomers), nitric acid (Chemsolute, 65% puriss.), and KOH (Chemsolute, ≥85%) were used as obtained without further purification. Aqueous solutions were prepared with ultrapure (Milli-Q) water. An amount of 1.563 g activated carbon was impregnated with 2000 µL of aqueous metal nitrate solution containing each 3 M total A-cation (La/Sr) and 3 M total B-cation (Ni/Fe) concentration. The impregnated carbon was heated with a 2 K min^{-1} ramp at 800°C for 1 h in stagnant air. The resulting powder was ground in an agate mortar. XRDs were measured from the obtained catalyst samples using Cu K_α radiation (Bruker D2 PHASER) in a range of $2\theta = 10°–90°$ in steps of 0.02°. Electron micrographs were recorded with a COXEM EM30-AXN tabletop SEM from gold-sputtered powder samples.

2.2 | Electrode Preparation and Electrochemical Evaluation

Catalyst inks are prepared by dispersing the catalysts powders in terpineol (200 mg mL^{-1}) via sonification for 15 min and vortexing. For the preparation of the Ni-substrate, an area of 1 cm^2 was unidirectionally polished with SiC-paper (grit 600). After cleaning with absolute ethanol, the Ni-substrate was etched for 4 min in concentrated nitric acid to increase its surface roughness to allow for a better catalyst adhesion. The substrate was subsequently washed with ultrapure water. A volume of 5 µL catalyst ink is dropcasted onto the as-prepared Ni-substrate surface. The coated electrodes are heated with a rate of 10 K min^{-1} to 600°C for 1 h in order to remove the terpineol and increase the mechanical binding of the catalyst to the Ni-substrate. The electrochemical performance of the different catalysts was tested and recorded in a three-electrode-setup consisting of the coated nickel working electrode (WE), a Hg/HgO (1 M KOH, ALS Co., Ltd. RE 61AP) reference electrode (RE), and a glassy carbon counter electrode (CE) with 1 M KOH as electrolyte at room temperature connected to a potentiostat/galvanostat (Metrohm PGSTAT204).

Initially, the WE surfaces were conditioned by 30 cyclic voltammograms (CVs) from −0.115 to 0.785 V versus Hg/HgO (1 M KOH) at a scan rate of 100 mV s^{-1}. The electrocatalytic activity of the coated Ni-WEs was then determined from the forward scan of the third out of three consecutive CVs recorded from 0.085 to 1.085 V versus Hg/HgO (1 M KOH) with 10 mV s^{-1}. For evaluation, all potentials applied or recorded by the potentiostat E_{pstat} were iR-corrected and referenced to the reversible hydrogen electrode (RHE) by adding the constant Hg/HgO (1 M KOH) RE potential of 0.915 V versus RHE. The potential E_{RHE} referenced against the RHE is obtained according to the following equation, where i is the current, and R_u the uncompensated resistance which was determined via electrochemical impedance spectroscopy (EIS):

$$E_{\mathrm{RHE}} = E_{\mathrm{pstat}} + 0.915\mathrm{V} - i \times R_u \quad (2)$$

The EISs were recorded at 1.6 V versus RHE with a root mean square perturbation potential amplitude of 10 mV for 10 frequencies per decade between 100 kHz and 0.1 Hz. Galvanostatic electrolysis (GE) measurements were performed with a glassy carbon CE and no RE at an applied current density of 10 mA cm^{-2} in relation to the geometric area of the WE.

3 | Results and Discussion

3.1 | Catalyst Characterization

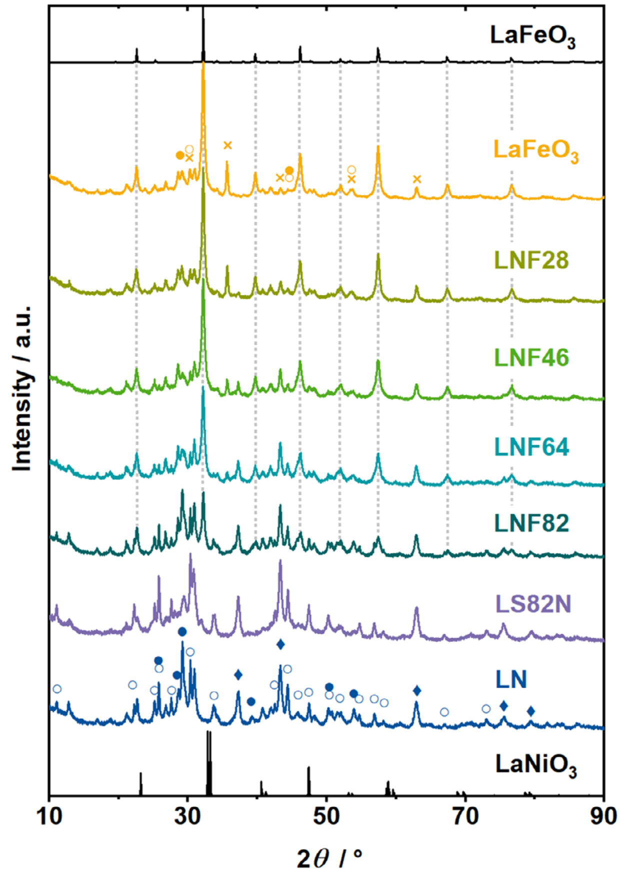

FIGURE 1 | X-ray diffractograms (XRD) of all prepared catalysts with reference XRDs of $LaNiO_3$ (ICSD-93919) and $LaFeO_3$ (ICSD-28255) both in black. Further observable phases are NiO (◆, ICSD-9866), La_2O_3 (●, ICSD-7795), $La_2O_2(CO_3)$ (○, ICSD-202988), and Fe_3O_4 (×, ICSD-77588).

The XRD of the sample prepared with the activated carbon impregnated by only La and Ni nitrates ($x = 0$, LN) as shown in Figure 1 reveals basically no reflexes of the desired $LaNiO_3$-phase, rendered from the inorganic crystal structure database [43] entry ICSD-93919 [44], but various other reflexes. The most intensive reflex at $2\theta = 29.2°$ can be assigned to the (1 0 1) and (0 1 1) planes of a trigonal La_2O_3 phase (*P*-3*m*1, ICSD-7795 [45]) with further reflexes at $2\theta = 28.4°$ and 25.8° attributable to the (0 0 2) and (1 0 0) planes, respectively. Several further reflexes indicate the presence of a hexagonal $La_2O_2(CO_3)$ phase ($P6_3$/mmc, ICSD-202988 [46]) with the second most intensive reflex at 30.4° 2θ attributable to the (1 0 3) plane. To this phase, the reflexes at $2\theta = 25.8°$, 44.4°, and 47.4° can be assigned to the (1 0 1), (1 1 0), and (1 0 7) planes as well. Furthermore, it appears that most of the nickel in this sample is present in the form of NiO, as multiple reflexes, including those at $2\theta = 37.2°$, 43.3°, 62.9°, 75.5°, and 79.4°, are in good agreement with each the (1 1 1), (2 0 0), (2 2 0), (3 1 1), and (2 2 2) planes of a cubic NiO phase (*Fm*-3*m*, ICSD-9866 [47]). The absence of reflexes attributable to a perovskite phase implies no formation of $LaNiO_3$ and, thus, the calcination of the metal nitrate precursors to the respective unary oxides. Furthermore, the formation of $La_2O_2(CO_3)$ could be explained by phases formed through the incomplete combustion of the carbon. Thus, the LN sample can be described as $La_2O_{3-y}(CO_3)_y$–NiO with $0 < y < c1$.

The XRD of $LaFeO_3$ on the other hand reveals reflexes at $2\theta = 22.5°$, 32.2°, 39.7°, 46.1°, 51.9°, 57.4°, 67.4°, and 76.6° which coincide well with those of the (0 0 2), (0 2 0), (0 2 2), (2 2 0), (2 2 2), (0 2 4), (2 2 4), and (2 4 0) planes respectively of an orthorhombic $LaFeO_3$ phase (*Pbnm*, ICSD-28255 [48]). Additionally, less intensive reflexes can be assigned to a cubic Fe_3O_4 phase (*Fm*-3*m*, ICSD-77588 [49]) with the reflexes at $2\theta = 30.2°$, 35.6°, 53.5°, and 62.8° attributable to the (2 2 0), (3 1 1), (4 2 2), and (4 4 0) planes. To similarly small extent, reflexes resulting from La_2O_3 are observable here which indicate small amounts of unmixed Fe- and La-species. Nevertheless, it can be concluded that the $LaFeO_3$ perovskite is successfully formed as the main phase for this sample. With decreasing Fe-content from LNF28 to LNF82 ($x = 0.8$, 0.6, 0.4, and 0.2), the relative intensity of the reflexes corresponding to the $LaFeO_3$ phase also decreases, whereas the reflexes corresponding to the $La_2O_{3-y}(CO_3)_y$–NiO-phases increase. Furthermore, no shift of the most intensive reflex of the $LaFeO_3$ phase at 32.2° toward the most intensive reflexes of the $LaNiO_3$ perovskite phase at 32.8° and 33.2° is visible. This shift would indicate a successful mixing of Ni and Fe on the B-site of the perovskite phase [31]. Hence, this implies the formation of pure, unsubstituted $LaFeO_3$ mixed together with the different phases found in LN, forming $(LaFeO_3)_x(La_2O_{3-y}(CO_3)_y\text{–NiO})_{1-x}$ mixtures.

The electron micrographs of LN (Figure 2a,b) and $LaFeO_3$ (Figure 2c,d) show irregularly shaped particles with a wide range of particle sizes from the nanometer scale to the 100 µm scale. All particles show very rough surfaces which implies the successful synthesis of catalysis particles with large surface area to allow for optimized catalyst utilization.

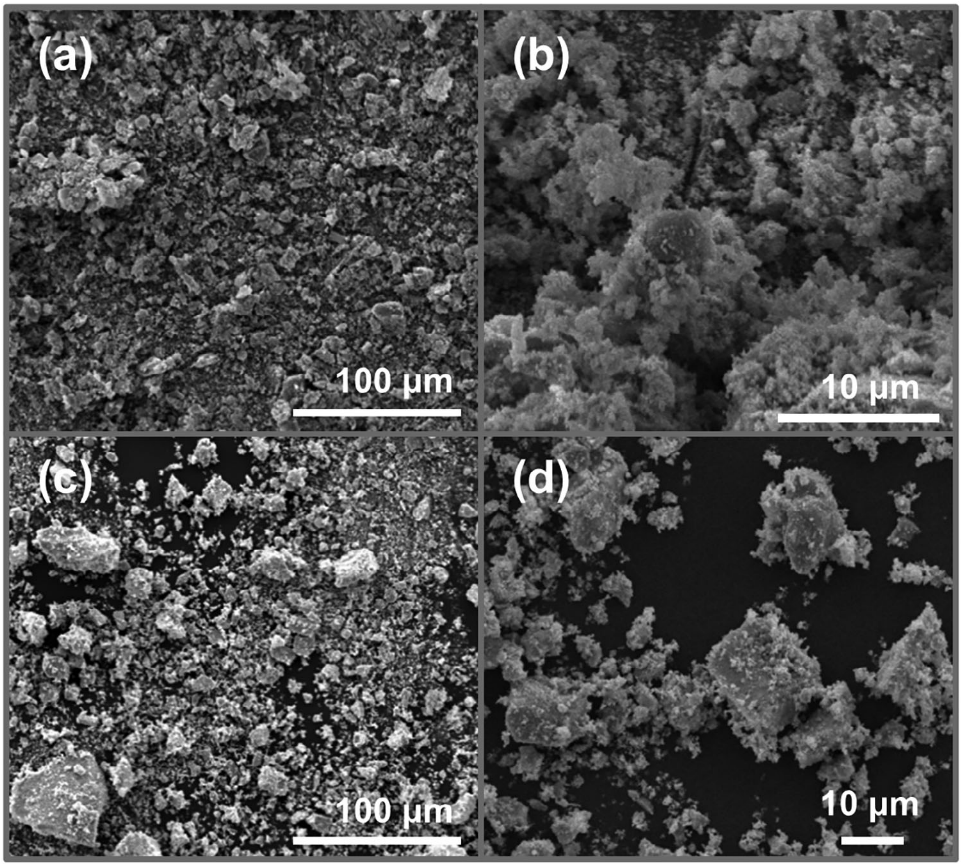

FIGURE 2 | Electron micrographs at different magnifications of (a and b) LN as well as (c and d) $LaFeO_3$.

3.2 | Evaluation of the Electrochemical Performance

As described in the experimental section, all samples were coated onto Ni-substrates before investigating the OER performance in 1 M KOH electrolyte. A total of 30 CVs were then recorded between 0.8 and 1.7 V versus RHE to condition the electrode surfaces. Subsequently, the electrocatalytic activity is then determined from the forward scans of CVs reaching higher into the OER overpotential region (>1.23 V vs. RHE) as shown in Figure 3a,b. At lower potentials, no chemical reaction is taking place as only very low currents are reached for all samples. For potentials higher than 1.23 V versus RHE, such low currents imply activation barriers in the OER which require higher potentials to be overcome. Above 1.5 V versus RHE, all samples show an increase in current at different rates. The lowest OER-onset potential can be found for LNF64 at about 1.55 V versus RHE. Higher activity in the OER-electrocatalysis equals higher current densities j reached at a given applied potential. Figure 3a shows a trend of increasing activity from LN, which reaches a maximum current of about 63 mA cm^{-2} to LNF82 reaching about 77 mA cm^{-2} with the highest activity obtained for LNF64 reaching about 94 mA cm^{-2}. With further increasing the Fe-content, the activity decreases from LNF46 to LNF82, which exhibit activities slightly lower than that of LNF82 and LN, respectively. The lowest activity is found for $LaFeO_3$. As the $LaNiO_3$ perovskite phase is not formed, a structure-related explanation of the activity difference between LN and $LaFeO_3$ is difficult. Nevertheless, NiO is identified as one of the main phases of the LN sample, and NiO_x-phases are well reported to exhibit high OER catalytic activity itself [12, 14, 25]. Furthermore, the literature-known enhancement of activity in presence of Fe can be observed here [23–26]. With a further increasing percentage of Fe present, however, the activity decreases below that of LN as mainly iron-based OER electrocatalysts are well-reported to exhibit lower activity than nickel-based OER electrocatalysts [12, 21, 25]. In Figure 3b, the performance of equally treated but uncoated Ni-substrate is included to allow for the estimation of the catalytic effect of the coatings on the Ni-substrate. Indeed, this catalytic effect is observable as the current densities reached with uncoated Ni are the lowest among all samples. Furthermore, Figure 3b shows a higher activity for the Sr-mixed LS82N sample in comparison to LN, reaching to about 85 mA cm^{-2}, which confirms the synergistic effect of mixing Sr into a Ni-based oxide—even without the presence of the main $LaNiO_3$ perovskite phase.

One benchmarking value to quantify and compare the activity of OER-electrocatalysts is the overpotential η which describes the additional potential needed to be applied in order to reach a certain current density in comparison to the OER equilibrium potential of 1.23 V versus RHE. In Figure 4, the overpotentials η_{10} which are needed to reach a current density of 10 mA cm^{-2} are compared. Here, the aforementioned catalytic effect of all coatings is well observable as the overpotentials of all coated electrodes are lower than that of uncoated Nickel with 501 mV. The trend of an initially decreasing and then increasing activity with increasing Fe-content is also observable well. The lowest overpotential is reached with LNF64 at 386 mV, and thus, this

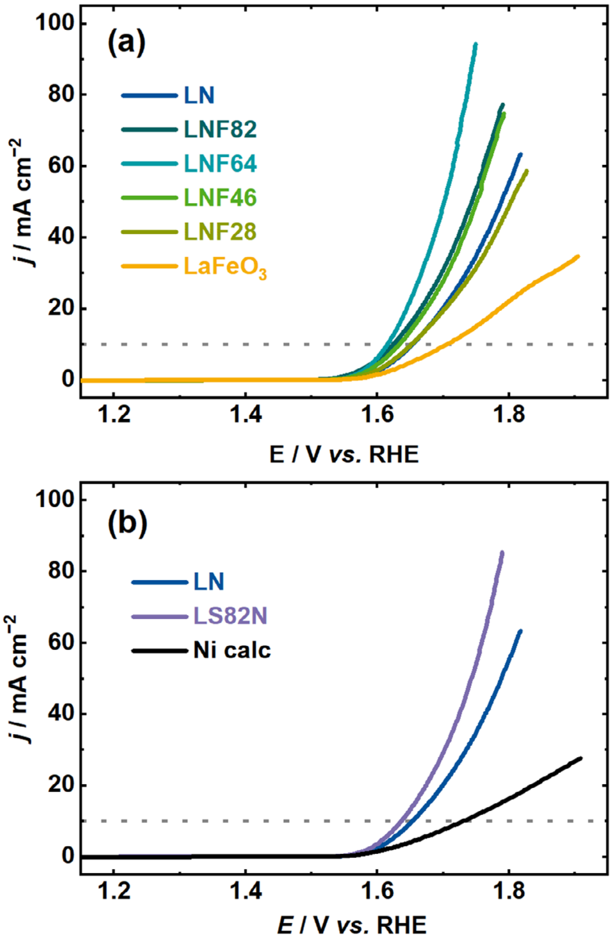

FIGURE 3 | iR-corrected forward scans of the cyclic voltammograms of (a) LN and all Fe-containing samples as well as (b) LN, LS82N and uncoated Ni-substrate (Ni calc) recorded at a scan rate of 10 mV s^{-1} in 1 M KOH against a Hg/HgO (1 M KOH) RE and a glassy carbon CE. The dotted horizontal lines depict the current density of 10 mA cm^{-2} where the overpotential is determined. CE, counter electrode; RE, reference electrode; RHE, reversible hydrogen electrode.

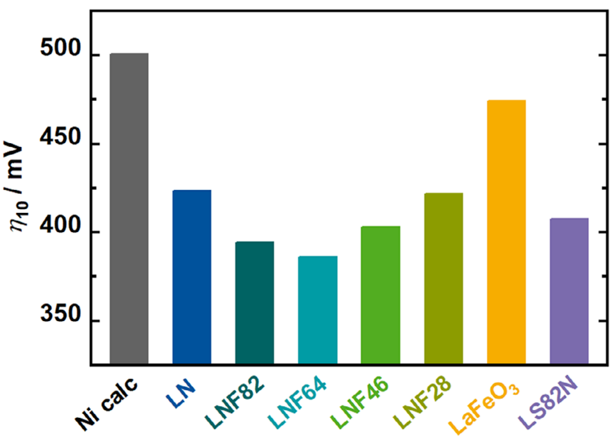

FIGURE 4 | Overpotentials η_{10} determined at a current density of 10 mA cm^{-2} for all samples and uncoated Ni.

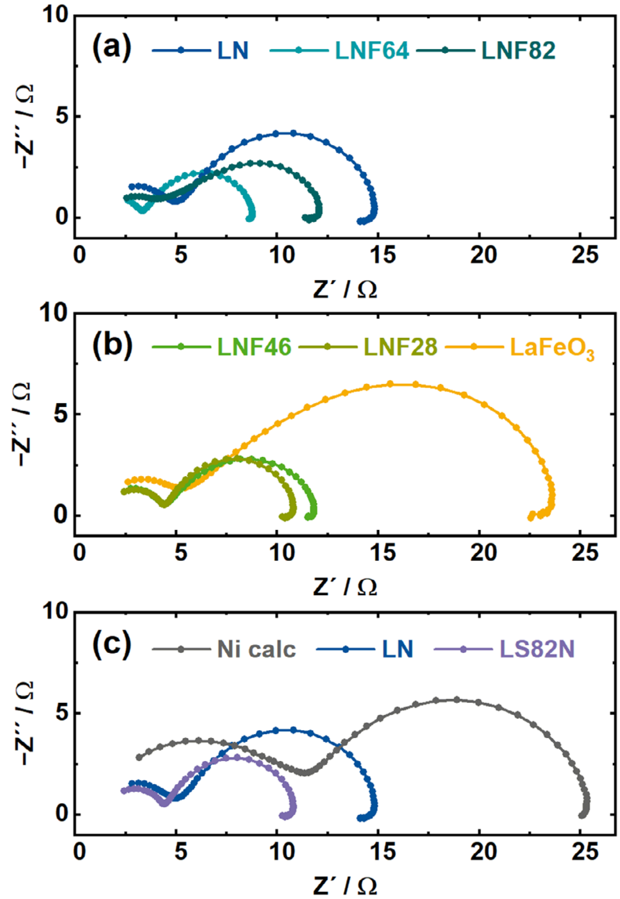

FIGURE 5 | Nyquist plots of the EIS recorded at an applied potential of 1.6 V versus RHE for (a and b) La–Ni–Fe-oxide-based samples as well as for (c) uncoated Ni as reference and LS82N. EIS, electrochemical impedance spectra; RHE, reversible hydrogen electrode.

ratio of Ni to Fe yields the highest electrocatalytic OER activity among all tested compositions. This confirms the synergistic effect of mixing Fe into Ni-based catalysts as reported in the literature [24–26, 35].

EIS allows an insight into electrochemical reaction parameters by comparing the frequency-dependent impedance behavior of the electrochemical system to that of an equivalent circuit. The parameters of the equivalent circuit elements can then be assigned to corresponding reaction parameters [50]. One important reaction parameter here is the charge transfer resistance R_{ct} which describes the resistance needed to be overcome when transferring charge between the electron-conducting electrode and the ion-conducting electrolyte across the phase boundary [50]. In a simplified perspective, typical electrochemical reactions show semicircles in the EIS Nyquist plots which are characterized by Randles equivalent circuits consisting of a resistor and a capacitor in parallel [50]. The resistor in this Randles circuit characterizes R_{ct} and can be quantified as the width of the semicircle and, thus, as the difference between the two x-axis intercepts [50]. Among other factors, the charge transfer resistance impacts the activity of electrocatalysts as resistances hinder the flow of current and, thus, the electrochemical reaction itself. Figure 5a–c shows the Nyquist plots of the impedance spectra of all catalysts and of uncoated Ni as reference. Here, all spectra show two consecutive semicircles with the first one being unequally pronounced. This implies the presence of two separate electrochemical processes [51]. One process can be assigned to the charge transfer between the electrode surface and the electrolyte resulting from the electrochemical OER taking place. As the EIS of uncoated Ni shows the most pronounced first semicircle, it can be concluded that the other electrochemical process does not result from the catalyst coating itself. Upon heating the coated and uncoated Ni-substrates at 600°C in stagnant air and, thus, an oxygen-containing atmosphere before the electrochemical measurements, the Ni-substrates develop a darker appearance, indicating the formation of a NiO-surface layer. Therefore, the first semicircle could be assigned to the process of charge transfer across this NiO-layer. Subsequently, the charge transfer resistance of all samples can be estimated from the width of the second semicircles. In Figure 5a, decreasing widths of these semicircles from LN to LNF64 are visible. Thus, the R_{ct} values show an inverse trend to the activity of the different catalysts. Figure 5b then shows an increasing trend from LNF46 to $LaFeO_3$. The lower R_{ct} of LS82N assessable in Figure 5c corresponds to its higher activity in comparison to LN, whereas uncoated Ni shows a larger R_{ct}.

In order to estimate the stability of the catalyst materials, Ni-substrates coated with LN, $LaFeO_3$, and LNF64 were applied in GE at 10 mA cm^{-2} for 3 h. XRDs of the coated electrodes were compared before and after GE as shown in Figure 6. The most intensive reflexes for all samples before and after GE at $2\theta = 44.5°$, 51.9°, and 76.4° can be assigned to the (111), (2 0 0), and (2 2 0) planes of a cubic Ni-phase (*Fm*-3*m*, ICSD-37502 [52]) and, thus, derive from the metallic Ni-substrate on which the samples are applied to. The two most intensive reflexes of a cubic NiO-phase at $2\theta = 37.2°$ (111) and 43.3° (2 0 0) can be found in Figure 6a in the XRDs of the Ni-free $LaFeO_3$-coated electrode which are absent in the $LaFeO_3$ powder XRD shown in Figure 1. This confirms the formation of a NiO-layer on the Ni-substrate upon heating of the coated electrodes as mentioned earlier. Along with the reflexes of metallic Ni, Figure 6b shows all observable reflexes of the $La_2O_{3-y}(CO_3)_y$–NiO-phases as found in Figures 1 and 6c all reflexes of the phases present in LNF64 both before and after GE. The main difference between the diffractograms is the loss in relative intensity of the reflexes after GE compared to those recorded beforehand. This can mainly be attributed to mechanical instability in form of loss of catalyst from the substrate as the adhesion of the catalyst layer is still subject to optimization. However, as the reflex positions of each sample remain consistent, it can be concluded that the catalysts remain chemically stable and no different phases are formed. This implies the stability of the catalyst coating under the applied GE conditions in 1 M KOH at room temperature for the duration of 3 h.

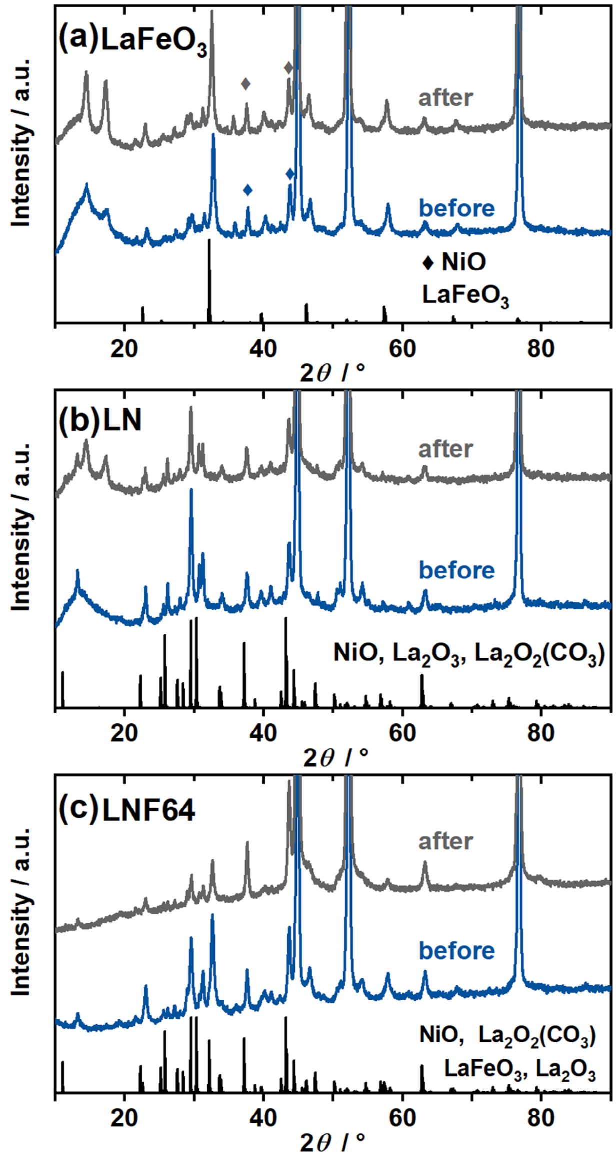

FIGURE 6 | XRDs of (a) $LaFeO_3$-coated, (b) LN-coated, and (c) LNF64-coated Ni-electrodes before (blue) and after (grey) 3 h of galvanostatic electrolysis at 10 mA cm^{-2}. The reference XRDs of the main phases of each catalyst are included in black. ♦ denotes the reflexes attributable to the formed NiO-surface layer on the electrodes. XRD, X-ray diffractometry.

4 | Conclusion

In this work, catalyst-coated Ni-substrate electrodes were prepared for the electrocatalysis of the OER in alkaline water splitting. The catalysts were synthesized by a facile preparation method in which highly porous activated carbon is impregnated by dissolved metal nitrate precursors. Upon heating the impregnated carbon, the precursors are calcined, and simultaneously, the templating carbon is removed. XRD studies of the products reveal a mixture consisting mainly of the unary oxides upon the impregnation with La- and Ni-nitrates described as $La_2O_{3-y}(CO_3)_y$–NiO. The impregnation with La- and Fe- on the other hand leads to the formation of a $LaFeO_3$ perovskite phase. All samples were coated onto Ni-substrates to be investigated in the alkaline OER electrocatalysis. Here, all samples show a catalytic effect on the OER as the activity of uncoated Ni is lower than for all coated Ni-electrodes. The electrochemical performances of the Ni–Fe-mixed samples show a trend of initially increasing and then decreasing activity with the lowest overpotential and, thus, highest activity found for LNF64. This confirms the literature-known synergistic effect of the presence of Fe on Ni-based OER electrocatalysts. Sr-mixing (LS82N) also results in a higher activity than LN, confirming the beneficial effect of Sr to the La–Ni-oxidic catalyst material despite the absence of a perovskite phase. EIS reveals that the charge transfer resistances of all tested samples follow the respective OER activity trends.

To conclude, this work successfully combines a facile synthesis protocol [36] of OER catalysts based on literature-known high-performing materials with directly implementing industrially relevant conditions by coating Ni-substrates as base electrodes in order to demonstrate a direct approach of preparing and testing technically relevant water splitting anodes.

Nomenclature

E	electric potential/V
i	electric current/A
j	current density/mA cm^{-2}
R	resistance/Ω
Z	electric impedance/Ω
η	overpotential/mV
θ	angle between incident X-ray and crystal lattice plane/°

Acknowledgments

We gratefully acknowledge funding of this project by the Federal Ministry of Education and Research (H2Giga QT1.1 PrometH2eus; FKZ 03HY105A). We also thank Noah Avraham-Radermacher for the XRD measurements.

Open access funding enabled and organized by Projekt DEAL.

Data Availability Statement

The data that support the findings of this study are available from the corresponding author upon reasonable request.

References

1. M. Momirlan and T. N. Veziroglu, "The Properties of Hydrogen as Fuel Tomorrow in Sustainable Energy System for a Cleaner Planet," *International Journal of Hydrogen Energy* 30, no. 7 (2005): 795–802.

2. N. Armaroli and V. Balzani, "The Hydrogen Issue," *ChemSusChem* 4, no. 1 (2011): 21–36.

3. G. Marbán and T. Valdés-Solís, "Towards the Hydrogen Economy?," *International Journal of Hydrogen Energy* 32, no. 12 (2007): 1625–1637.

4. L. Barreto, A. Makihira, and K. Riahi, "The Hydrogen Economy in the 21st Century: A Sustainable Development Scenario," *International Journal of Hydrogen Energy* 28, no. 3 (2003): 267–284.

5. N. M. Dowell, N. Sunny, N. Brandon, et al., "The Hydrogen Economy: A Pragmatic Path Forward," *Joule* 5, no. 10 (2021): 2524–2529.

6. T. E. Mallouk, "Divide and Conquer," *Nature Chemistry* 5, no. 5 (2013): 362–363.

7. H. Dau, C. Limberg, T. Reier, M. Risch, S. Roggan, and P. Strasser, "The Mechanism of Water Oxidation: From Electrolysis via Homogeneous to Biological Catalysis," *ChemCatChem* 2, no. 7 (2010): 724–761.

8. M. Yu, E. Budiyanto, and H. Tüysüz, "Principles of Water Electrolysis and Recent Progress in Cobalt-, Nickel-, and Iron-Based Oxides for the Oxygen Evolution Reaction," *Angewandte Chemie International Edition* 61, no. 1 (2022): e202103824.

9. R. Eisenberg and H. B. Gray, "Preface on Making Oxygen," *Inorganic Chemistry* 47, no. 6 (2008): 1697–1699.

10. S. Anwar, F. Khan, Y. Zhang, and A. Djire, "Recent Development in Electrocatalysts for Hydrogen Production Through Water Electrolysis," *International Journal of Hydrogen Energy* 46, no. 63 (2021): 32284–32317.

11. C. C. L. McCrory, S. Jung, I. M. Ferrer, S. M. Chatman, J. C. Peters, and T. F. Jaramillo, "Benchmarking Hydrogen Evolving Reaction and Oxygen Evolving Reaction Electrocatalysts for Solar Water Splitting Devices," *Journal of the American Chemical Society* 137, no. 13 (2015): 4347–4357.

12. S. Trasatti, "Electrocatalysis by Oxides—Attempt at a Unifying Approach," *Journal of Electroanalytical Chemistry and Interfacial Electrochemistry* 111, no. 1 (1980): 125–131.

13. Y. Matsumoto and E. Sato, "Electrocatalytic Properties of Transition Metal Oxides for Oxygen Evolution Reaction," *Materials Chemistry and Physics* 14, no. 5 (1986): 397–426.

14. C. C. L. McCrory, S. Jung, J. C. Peters, and T. F. Jaramillo, "Benchmarking Heterogeneous Electrocatalysts for the Oxygen Evolution Reaction," *Journal of the American Chemical Society* 135, no. 45 (2013): 16977–16987.

15. M. E. Lyons and M. P. Brandon, "A Comparative Study of the Oxygen Evolution Reaction on Oxidised Nickel, Cobalt and Iron Electrodes in Base," *Journal of Electroanalytical Chemistry* 641, no. 1–2 (2010): 119–130.

16. J. S. Kim, B. Kim, H. Kim, and K. Kang, "Recent Progress on Multimetal Oxide Catalysts for the Oxygen Evolution Reaction," *Advanced Energy Materials* 8, no. 11 (2018): 1702774.

17. F. Zeng, C. Mebrahtu, L. Liao, A. K. Beine, and R. Palkovits, "Stability and Deactivation of OER Electrocatalysts: A Review," *Journal of Energy Chemistry* 69 (2022): 301–329.

18. J. Hwang, R. R. Rao, L. Giordano, Y. Katayama, Y. Yu, and Y. Shao-Horn, "Perovskites in Catalysis and Electrocatalysis," *Science* 358, no. 6364 (2017): 751–756.

19. A. S. Bhalla, R. Guo, and R. Roy, "The Perovskite Structure—A Review of its Role in Ceramic Science and Technology," *Materials Research Innovations* 4, no. 1 (2000): 3–26.

20. X. Xu, W. Wang, W. Zhou, and Z. Shao, "Recent Advances in Novel Nanostructuring Methods of Perovskite Electrocatalysts for Energy-Related Applications," *Small Methods* 2, no. 7 (2018): 1800071.

21. J. Suntivich, H. A. Gasteiger, N. Yabuuchi, H. Nakanishi, J. B. Goodenough, and Y. Shao-Horn, "Design Principles for Oxygen-Reduction Activity on Perovskite Oxide Catalysts for Fuel Cells and Metal-Air Batteries," *Nature Chemistry* 3, no. 7 (2011): 546–550.

22. J. O. Bockris and T. Otagawa, "Mechanism of Oxygen Evolution on Perovskites," *Journal of Physical Chemistry* 87, no. 15 (1983): 2960–2971.

23. S. Anantharaj, S. Kundu, and S. Noda, "The Fe Effect: A Review Unveiling the Critical Roles of Fe in Enhancing OER Activity of Ni and Co Based Catalysts," *Nano Energy* 80 (2021): 105514.

24. D. A. Corrigan, "The Catalysis of the Oxygen Evolution Reaction by Iron Impurities in Thin Film Nickel Oxide Electrodes," *Journal of the Electrochemical Society* 134, no. 2 (1987): 377–384.

25. L. Trotochaud, J. K. Ranney, K. N. Williams, and S. W. Boettcher, "Solution-Cast Metal Oxide Thin Film Electrocatalysts for Oxygen Evolution," *Journal of the American Chemical Society* 134, no. 41 (2012): 17253–17261.

26. L. Trotochaud, S. L. Young, J. K. Ranney, and S. W. Boettcher, "Nickel–Iron Oxyhydroxide Oxygen-Evolution Electrocatalysts: The Role of Intentional and Incidental Iron Incorporation," *Journal of the American Chemical Society* 136, no. 18 (2014): 6744–6753.

27. R. Chiba, F. Yoshimura, and Y. Sakurai, "An Investigation of $LaNi_{1-x}Fe_xO_3$ as a Cathode Material for Solid Oxide Fuel Cells," *Solid State Ionics* 124, no. 3–4 (1999): 281–288.

28. D. Zhang, Y. Song, Z. Du, L. Wang, Y. Li, and J. B. Goodenough, "Active $LaNi_{1-x}Fe_xO_3$ Bifunctional Catalysts for Air Cathodes in Alkaline Media," *Journal of Materials Chemistry A* 3, no. 18 (2015): 9421–9426.

29. C. B. Gozzo, M. R. Soares, J. C. Sczancoski, I. C. Nogueira, and E. R. Leite, "Investigation of the Electrocatalytic Performance for Oxygen

Evolution Reaction of Fe-Doped Lanthanum Nickelate Deposited on Pyrolytic Graphite Sheets," *International Journal of Hydrogen Energy* 44, no. 39 (2019): 21659–21672.

30. J. Bak, H. Bin Bae, and S.-Y. Chung, "Atomic-Scale Perturbation of Oxygen Octahedra via Surface Ion Exchange in Perovskite Nickelates Boosts Water Oxidation," *Nature Communications* 10, no. 1 (2019): 2713.

31. L. Wang, P. Adiga, J. Zhao, et al., "Understanding the Electronic Structure Evolution of Epitaxial $LaNi_{1-x}Fe_xO_3$ Thin Films for Water Oxidation," *Nano Letters* 21, no. 19 (2021): 8324–8331.

32. J. Q. Adolphsen, B. R. Sudireddy, V. Gil, and C. Chatzichristodoulou, "Oxygen Evolution Activity and Chemical Stability of Ni and Fe Based Perovskites in Alkaline Media," *Journal of the Electrochemical Society* 165, no. 10 (2018): F827–F835.

33. M. Li, A. R. Insani, L. Zhuang, et al., "Strontium-Doped Lanthanum Iron Nickelate Oxide as Highly Efficient Electrocatalysts for Oxygen Evolution Reaction," *Journal of Colloid and Interface Science* 553 (2019): 813–819.

34. Q. Guo, X. Li, H. Wei, et al., "Sr, Fe Co-Doped Perovskite Oxides with High Performance for Oxygen Evolution Reaction," *Frontiers in Chemistry* 7 (2019): 224.

35. K. Zhu, F. Shi, X. Zhu, and W. Yang, "The Roles of Oxygen Vacancies in Electrocatalytic Oxygen Evolution Reaction," *Nano Energy* 73 (2020): 104761.

36. J. T. Mefford, X. Rong, A. M. Abakumov, et al., "Water Electrolysis on $La_{1-x}Sr_xCoO_{3-\delta}$ Perovskite Electrocatalysts," *Nature Communications* 7 (2016): 11053.

37. Y. Matsumoto, S. Yamada, T. Nishida, and E. Sato, "Oxygen Evolution on $La_{1-x}Sr_xFe_{1-y}Co_yO_3$ Series Oxides," *Journal of the Electrochemical Society* 127, no. 11 (1980): 2360–2364.

38. Y. Takeda, R. Kanno, T. Kondo, et al., "Properties of SrMO 3-?(M=Fe, Co) as Oxygen Electrodes in Alkaline Solution," *Journal of Applied Electrochemistry* 12, no. 3 (1982): 275–280.

39. A. Wattiaux, J. C. Grenier, M. Pouchard, and P. Hagenmuller, "Electrolytic Oxygen Evolution in Alkaline Medium on $La_{1-x}Sr_xFeO_{3-y}$ Perovskite-Related Ferrites: I. Electrochemical Study," *Journal of the Electrochemical Society* 134, no. 7 (1987): 1714–1718.

40. J. Brauns and T. Turek, "Alkaline Water Electrolysis Powered by Renewable Energy: A Review," *Processes* 8, no. 2 (2020): 248.

41. D. E. Hall, "Electrodes for Alkaline Water Electrolysis," *Journal of the Electrochemical Society* 128, no. 4 (1981): 740–746.

42. M. Schwickardi, T. Johann, W. Schmidt, and F. Schüth, "High-Surface-Area Oxides Obtained by an Activated Carbon Route," *Chemistry of Materials* 14, no. 9 (2002): 3913–3919.

43. D. Zagorac, H. Müller, S. Ruehl, J. Zagorac, and S. Rehme, "Recent Developments in the Inorganic Crystal Structure Database: Theoretical Crystal Structure Data and Related Features," *Journal of Applied Crystallography* 52, no. Pt 5 (2019): 918–925.

44. J. C. Park, D. K. Kim, S. H. Byeon, and D. Kim, "XANES Study on Ruddlesden-Popper Phase, $La_{n+1}Ni_nO_{3n+1}$ (n = 1, 2, and ∞)," *Journal of Synchrotron Radiation* 8, no. Pt 2 (2001): 704–706.

45. C. Gökhan Ünlü, M. Burak Kaynar, T. Şimşek, A. Tekgül, B. Kalkan, and Ş. Özcan, "Structure and Magnetic Properties of $(La_{1-x}Fe)FeO_3$ (x = 0, 0.25, 0.50) Perovskite," *Journal of Alloys and Compounds* 784 (2019): 1198–1204.

46. J. Attfield and G. Férey, "Structure Determinations of La2O2CO3-II and the Unusual Disordered Phase $La_2O_{2.52}(CO_3)_{0.74}Li_{0.52}$ Using Powder Diffraction," *Journal of Solid State Chemistry* 82, no. 1 (1989): 132–138.

47. S. Sasaki, K. Fujino, and Y. Takéuchi, "X-ray Determination of Electron-Density Distributions in Oxides, MgO, MnO, CoO, and NiO, and Atomic Scattering Factors of Their Constituent Atoms," *Proceedings of the Japan Academy, Series B* 55, no. 2 (1979): 43–48.

48. M. Marezio and P. D. Dernier, "The Bond Lengths in $LaFeO_3$," *Materials Research Bulletin* 6, no. 1 (1971): 23–29.

49. L. W. Finger, R. M. Hazen, and A. M. Hofmeister, "High-Pressure Crystal Chemistry of Spinel ($MgAl_2O_4$) and Magnetite (Fe_3O_4): Comparisons with Silicate Spinels," *Physics and Chemistry of Minerals* 13, no. 4 (1986): 215–220.

50. A. J. Bard and L. R. Faulkner, *Electrochemical Methods—Fundamentals and Applications* (Hoboken: John Wiley & Sons, 2001).

51. A. Lasia, *Electrochemical Impedance Spectroscopy and Its Applications* (Singapore: Springer, 2014).

52. J. O. Conway and T. J. Prior, "Interstitial Nitrides Revisited—A Simple Synthesis of M Mo3N (M = Fe, Co, Ni)," *Journal of Alloys and Compounds* 774 (2019): 69–74.